Aerospace Science and Technology 88 (2019) 244–257

Contents lists available at ScienceDirect

Aerospace Science and Technology

www.elsevier.com/locate/aescte

Geometrically nonlinear static aeroelastic analysis of composite morphing wing with corrugated structures

Natsuki Tsushima [a,*], Tomohiro Yokozeki [b], Weihua Su [c], Hitoshi Arizono [a]

[a] Japan Aerospace Exploration Agency, Mitaka, Tokyo 181-0015, Japan
[b] Department of Aeronautics and Astronautics, University of Tokyo, Hongo, Tokyo 113-8656, Japan
[c] Department of Aerospace Engineering and Mechanics, University of Alabama, Box 870280, Tuscaloosa, AL 35487-0280, USA

ARTICLE INFO

Article history:
Received 14 December 2018
Received in revised form 22 February 2019
Accepted 8 March 2019
Available online 14 March 2019

Keywords:
Finite elements
Nonlinear analysis
Composites
Corrugated panel
Unsteady vortex-lattice method
Morphing wing

ABSTRACT

In this paper, an integrated geometrically nonlinear aeroelastic framework to analyze the static nonlinear aeroelastic response of morphing composite wing with orthotropic materials has been developed. A flat plate/shell finite element, which can model plate-like wings, has been accommodated to model composite/corrugated panels to investigate effects of different laminate orientations and corrugations. A corotational approach is used to consider the geometrical nonlinearity due to large deformation produced by wing morphing. An unsteady vortex-lattice method is implemented to couple with the structural model subject to the large deformations. A homogenization method is also implemented to model corrugated panels as equivalent orthotropic plates. Individual structural, aerodynamic, and corrugated panel models, as well as the complete nonlinear aeroelastic framework, are verified. Numerical studies explore the static aeroelastic responses of a flat wing with composite/corrugated panels. This work helps to understand the nonlinear aeroelastic characteristics of composite/corrugated wings and demonstrates the capability of the framework to analyze the nonlinear aeroelasticity of such morphing wings.

1. Introduction

Recently wing morphing has generated a good deal of attention as a potential technique to improve aircraft performance and to facilitate economic flight. The morphing technique can achieve the optimal flight performance in a wide range of operation conditions by adaptively changing the wing shape, even in-flight conditions in which conventional control surfaces decrease their performance. Specifically, the morphing technology may improve aerodynamic characteristics and reduce structural weight and acoustic noise of aircraft [1–5]. In addition, it may help to improve flight safety through enhancement of stall characteristics and gust alleviation.

Recently, many researchers have studied various morphing technologies to evaluate the performance of those morphing wings. One of the contemporary concepts taking advantage of such wing morphing technique is the Variable Camber Continuous Trailing Edge Flap system (VCCTEF) [4,6]. The VCCTEF adopted a flap system which was capable of changing flap angles in spanwise direction seamlessly. In addition, the system implemented three discrete control surface sections in chordwise direction contributing to distribute chordwise aerodynamic pressures smoothly. The performance of the VCCTEF system was evaluated based on aerodynamic numerical simulations and wind tunnel tests, and the results showed performance improvements with respect to drag reduction and high-lift up to 6.31%.

Examples of morphing wing technologies include conceptual designs utilizing smart materials corresponding to recent developments in smart structures and materials technologies. For instance, Adaptive Compliant Trailing Edge (ACTE) flap [2,3] was designed and tested by advantageously using the morphing concept and smart materials. The flaps can be actuated with piezoelectric materials, and the increase of lift and pitch moment owing to the ACTE flap has been proven in flight tests. Such piezoelectric-based morphing wings have the two advantages of fast response and high bandwidth. Morphing wings with piezoelectric materials are suitable to suppress aeroelastic instabilities and can extend the flight envelope [7–10]. However, the piezoelectric-based wing morphing requires very high energy to produce large deformation. Thus, it may not be the best suited for wing morphing requiring large deformations such as camber morphing, which is another way to improve aircraft performance.

At the same time, another morphing wing strategy using a simple wiring actuation mechanism with corrugated structures has been studied [11–13]. Due to the anisotropy of the structure, corrugated structures are stiffer in one direction and softer in an-

* Corresponding author.
E-mail address: tsushima.natsuki@jaxa.jp (N. Tsushima).

https://doi.org/10.1016/j.ast.2019.03.025
1270-9638/

Nomenclature

A = Element area, m^2
A_{ij}, D_{ij} = Membrane and bending components of stiffness for composite material
$\bar{A}_{ij}, \bar{D}_{ij}$ = Membrane and bending components of stiffness for equivalent orthotropic plate
B = Body frame
$\mathbf{B}$ = Coupling stiffness matrix
$\mathbf{B}_b, \mathbf{B}_m$ = Strain-displacement matrices of the DKT and OPT elements
b = Semi span of wing or length of beam, m
$\Delta b_k, \Delta c_k$ = Element chord and span on the kth panel, m
c = Chord length, m
C_L = Lift coefficient
Δc_{cor} = Element chord of corrugated panel, m
$\mathbf{D}^e$ = Flexural rigidity matrix of the DKT element
$\Delta\mathbf{D}$ = Displacement increment
$\mathbf{d}, \mathbf{d}_b, \mathbf{d}_m$ = Nodal displacement vectors of the flat plate/shell, DKT, and OPT elements
$\mathbf{E}$ = Elasticity matrix of the OPT element
E, E_0 = Current and initial frames of the triangular element
$\bar{E}$ = Young's modulus, GPa
F, M = Applied force and moment, N and N m
$\mathbf{F}_k$ = Aerodynamic load on the kth panel
$\mathbf{G}$ = Derivative component matrix of shape functions
G = Global frame
$\bar{G}$ = Shear modulus, GPa
$\mathbf{G}_s, \mathbf{G}_a$ = Interpolation matrices for structural displacement and aerodynamic load
h = Altitude, m
$\bar{h}, L, R, s$ = Geometric parameters of corrugated panel, m
I = Moment of inertia, m^4
I_1, I_2 = Functions of the corrugation geometry
$\bar{\mathbf{K}}, \bar{\mathbf{R}}$ = Assembled current stiffness matrix and load residual vector
$\mathbf{k}, \mathbf{k}_b, \mathbf{k}_m$ = Stiffness matrices of the flat plate/shell, DKT, and OPT elements
$\mathbf{k}_\sigma$ = Geometric stiffness matrix
$\mathbf{L}$ = Constant matrix of the OPT element
$\bar{\mathbf{N}}$ = Resultant load matrix
$\bar{N}, \bar{M}$ = Forces and moments of equivalent orthotropic plate, N and N m
$\mathbf{n}$ = Normal vector to the lifting surface
n_{LSc} = Number of chordwise discretization for the lifting panels
n_{cor} = Number of corrugation cycle
$\mathbf{P}$ = Projection matrix
Δp_k = Pressure difference between upper and lower surfaces to the kth panel, Pa
$\mathbf{r}$ = Internal force vector
$\mathbf{r}_m, \mathbf{r}_n, \mathbf{r}_0$ = Position vectors of vortex ring corners
S, S_0 = Current and initial nodal triads
S_k = Panel area, m^2
$\mathbf{T}, \mathbf{T}_E, \mathbf{T}_{E0}, \mathbf{T}_S$ = Transformation matrices
$\tilde{t}, \tilde{n}$ = Bases of local coordinate system for a corrugation
$\bar{t}$ = Thickness of the composite sheet forming the corrugation, m
t_p = Total thickness of the panel or thickness between the wing's upper and lower surfaces, m
U_∞ = Freestream velocity, m/s
u, v, w = Displacement components
$\mathbf{u}^B$ = Displacement vector of a node
$\bar{u}_i, \theta_i$ = Elastic nodal displacements and rotations at the ith node, m and rad
V = Element volume, m^3
$\mathbf{v}$ = Lifting surface velocity
$\mathbf{w}_{ij}$ = Induced flow velocity on the ith bound vortex influenced by the jth vortex ring
$\mathbf{w}_{si}, \mathbf{w}_{ai}$ = Deflections at each grid in the structural and aerodynamic coordinates
$\mathbf{w}_w$ = Induced flow velocity due to the wake
$\mathbf{X}^G$ = Position of the body frame's origin in the global frame
$\mathbf{X}^B, \mathbf{x}^B$ = Initial and current positions of a node in the body frame
X_a, Y_a, Z_a = Aerodynamics coordinate
$\Delta\mathbf{x}_w$ = Movement of each shed wake
Γ, Γ_w = Circulation of the bound and wake vortices
α = Angle of attack, deg
$\varepsilon, \gamma, \kappa$ = Strains and curvatures of the composite material at the mid-plane
$\bar{\varepsilon}, \bar{\gamma}, \bar{\kappa}$ = Strains and curvatures of the orthotropic plate at the mid-plane
$\zeta_1, \zeta_2, \zeta_3$ = Natural coordinates of elements
$\theta_x, \theta_y, \theta_z$ = Rotational components, rad
$\tilde{\theta}_x, \tilde{\theta}_y, \tilde{\theta}_z$ = Incremental rotations of triad S in the body frame, rad
ν = Poisson's ratio
ρ = Density, kg/m^3
$\boldsymbol{\tau}_x, \boldsymbol{\tau}_y$ = Panel tangential vectors in the x and y directions
Φ_B, Φ_w = Potential of the bound elements and shed wake

other direction. The dual functions of a morphing wing, including spanwise load bearing and chordwise morphing, are therefore possible by taking advantage of the extremely anisotropic property of corrugated structures. One advantage of the corrugated morphing scheme is that it is easy to fabricate corrugated structures. Additionally, corrugated structures can be actuated simply with commercially available actuators and wires although other driving methods may also be adopted. Therefore, the mechanism with corrugated structures may be applicable for camber morphing. However, to realize an efficient corrugated-based camber morphing, improvement of aerodynamic characteristics and adaptivity to flight condition with the corrugated morphing wing should be adequately evaluated. In addition, a proper method to accurately consider composite and corrugated structures is needed for the evaluations. Xia et al. proposed a homogenization method to describe corrugated structures as equivalent orthotropic panels [14]. If the method is integrated with a flat plate/shell finite element, the integrated structural model will allow the structural analysis of the corrugated structures.

Morphing technology aims to achieve very efficient aerodynamic and structural designs (configuration) by actively altering wing geometry during flight, which contribute to the high performance of aircraft. The morphing wings may undergo large deformations but small strains due to the wing morphing, resulting in geometrically nonlinear deformations, limit-cycle oscillations (LCOs), and so on. Hence, to accurately analyze morphing aircraft/wings, an aeroelastic model to consider the geometrical nonlinearities is important. Moreover, wing morphing during flight also causes unsteady aerodynamic flows. Even though the accurate nonlinear aeroelastic analysis can be performed by using computational fluid dynamics (CFD) [15–18], it compromises computational efficiency, especially in case the large wing motion is involved.

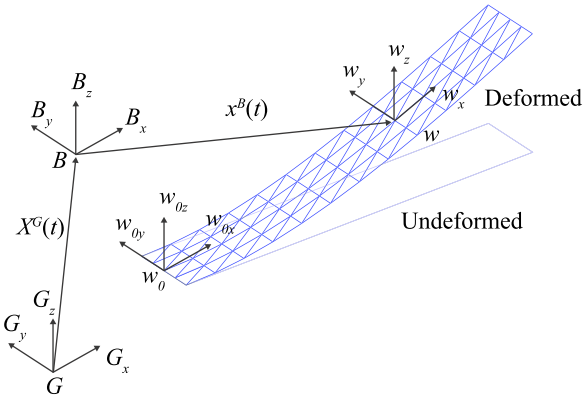

Fig. 1. Coordinate systems for the current framework.

As an alternative approach, an unsteady aerodynamic model can be coupled with a geometrically nonlinear finite element model for computational efficiency with adequately accurate solutions, which can be used for preliminary to middle stage of developments. Especially among different aerodynamic models used for problems subjected to the large deformations, an unsteady vortex-lattice method has shown to provide simplicity for implementation and computational cost reduction [19,20].

In this paper, a cost-effective geometrically nonlinear aeroelastic framework to analyze the static nonlinear aeroelastic response of composite morphing wing with corrugated structures has been developed. The objectives of this paper are 1) to develop an integrated geometrically nonlinear aeroelastic framework, which allows studying corrugated morphing wings, 2) to verify the developed analysis framework, and 3) to demonstrate the capability of the framework and explore the influence of different corrugated morphing wing designs on aeroelastic responses as well as the aeroelastic characteristics of corrugated camber morphing wings. For structural model, a corotational approach with flat plate/shell finite elements is used to take into account the geometrical nonlinearity due to the large deformation of morphing wing. The corotational approach has an advantage in effectiveness for solving problems with large deformation compared with other conventional nonlinear FEM. A UVLM formulation has also been implemented and coupled with the structural part. The integrated nonlinear aeroelastic framework also provides the capability to investigate the influence of different materials and structures. The present code allows studying the geometrically nonlinear aeroelastic response of both isotropic and orthotropic materials. The response of a corrugated structure, which is compatible with a camber morphing wing, can also be analyzed by approximating the structure as an equivalent orthotropic panel with a homogenization method. In addition, the spring element is implemented in the structural solver for additional modeling capability. Although the UVLM is implemented, a static analysis procedure of geometrically nonlinear aeroelasticity is developed in the current study as a basis of nonlinear and unsteady aeroelastic analysis framework development. The current model will then be extended to transient model in future works.

2. Theoretical formulation

The aeroelastic analysis is carried out in the current work to study composite flat wings undergoing large deflections. To properly describe wing morphing by corrugated structures, a corrugated panel model for the trailing edge (TE) portion of wings is implemented. Individual aerodynamic and structural models are implemented, and an interpolation method is used to couple both models.

2.1. Reference frames

To describe dynamics of aircraft with flexible lifting surfaces undergoing large translational and rotational motion during flights, a few coordinate systems are defined as the global frame G, the body frame B, and the local beam frame w. The different reference frames and coordinate systems are defined in Fig. 1. Bases of the local frame w are w_x, w_y, and w_z, whose directions are toward the wing tip, the leading edge (LE), and normal to the local surface, respectively. In addition, another coordinate system to solve aerodynamics for the moving surfaces is defined. Traditionally by using the Cartesian coordinate, the X_a, Y_a, and Z_a axes for the aerodynamics coordinate is defined along the flow direction ($-B_y$), toward the starboard (B_x), and normal to the plane made by the first two axes (B_z).

2.2. Interpolation between structural and aerodynamic coordinates

The communication of information between the structural and aerodynamics coordinates (lifting-surface deflections and aerodynamic loads) are handled by using the thin-plate spline (TPS) method [21], which assumes the surfaces of both structural and aerodynamic grids coincide. The TPS method can accurately interpolate the information and exhibits robustness for an analysis subjected to the large displacements [21].

Two different interpolations are involved in the process of the aeroelastic analysis. One is the transformation of the structural wing deformations into the aerodynamic panel deformations. The other is the transformation of the aerodynamic loads into the structurally equivalent loads exerted on the structural grids. Those interpolations are performed through interpolation matrices $\mathbf{G}_s$ and $\mathbf{G}_a$, respectively. Fig. 2 shows the transformations of structural displacements and aerodynamic loads. As shown in Fig. 2, the matrix $\mathbf{G}_s$ is constructed based on the grid points on each structural finite element and the grids and center points of each aerodynamic panel. The transformation matrix relates each component of structural deflection to aerodynamic deflection as

$$\mathbf{w}_{ai} = \mathbf{G}_s \mathbf{w}_{si} \tag{1}$$

where $\mathbf{w}_{si}$ is the deflections at each grid in the structural coordinate and $\mathbf{w}_{ai}$ is the deflections at each grid in the aerodynamic interpolation points. Similarly, the interpolation of the aerodynamic load to the structural coordinate can be performed. However, since the interpolation is from the collocation points located on three-quarter chord point of each aerodynamic panel to the grid on the structural coordinate, the matrix $\mathbf{G}_a$ is different from the matrix $\mathbf{G}_s$ and provides "structurally equivalent" loads rather than statically equivalent through the transformation.

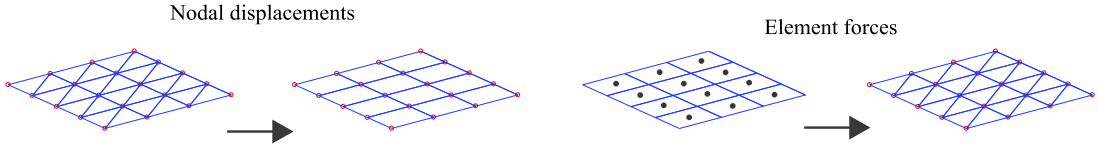

Fig. 2. Coordinate transformations of structural displacements and aerodynamic loads.

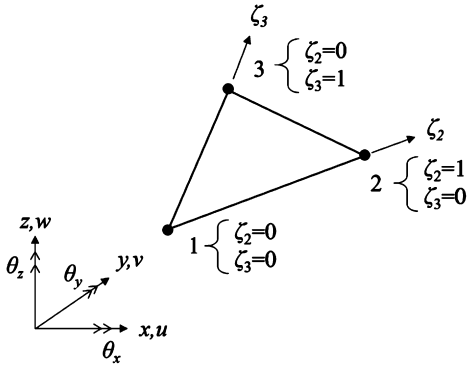

Fig. 3. Geometry of the triangular element.

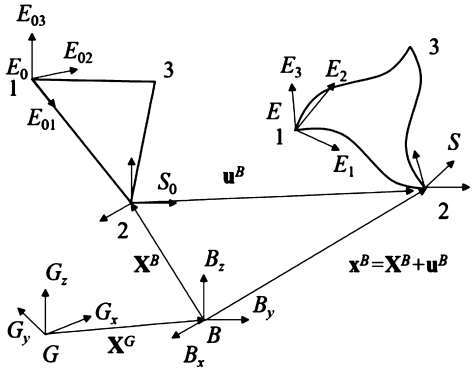

Fig. 4. System frames of the triangular element.

2.3. Structural model with flat plate/shell finite element using corotational approach

2.3.1. Triangular flat plate/shell finite element

The geometrically nonlinear structural dynamics is solved using three-node triangular flat plate/shell element. The flat plate/shell element is constructed by combining the optimal triangle membrane (OPT) [22,23] element and the discrete Kirchhoff triangle (DKT) [24] plate bending element. The geometry of a triangular flat plate/element is shown in Fig. 3. The nodal displacement vector $\mathbf{d}_m$ and stiffness matrix $\mathbf{k}_m$ of the OPT element are given as

$$\{\mathbf{d}_m\} = \left\{ u_1 \quad v_1 \quad \theta_{z1} \quad u_2 \quad v_2 \quad \theta_{z2} \quad u_3 \quad v_3 \quad \theta_{z3} \right\}^T \tag{2}$$

$$[\mathbf{k}_m] = \frac{1}{V}\mathbf{L}\mathbf{E}\mathbf{L}^T + \int_\Omega \mathbf{B}_m^T \mathbf{E}\mathbf{B}_m dA \tag{3}$$

where V is the element volume, $\mathbf{E}$, $\mathbf{B}_m$, and $\mathbf{L}$ are the elasticity, strain-displacement, and constant matrices, respectively. The integration is calculated using three Gauss points. The nodal displacement vector $\mathbf{d}_b$ and stiffness matrix $\mathbf{k}_b$ of the DKT element are given as

$$\{\mathbf{d}_b\} = \left\{ w_1 \quad \theta_{x1} \quad \theta_{y1} \quad w_2 \quad \theta_{x2} \quad \theta_{y2} \quad w_3 \quad \theta_{x3} \quad \theta_{y3} \right\}^T \tag{4}$$

$$[\mathbf{k}_b] = \int_\Omega \mathbf{B}_b^T \mathbf{D}^e \mathbf{B}_b dA = 2A \int_0^1 \int_0^{1-\zeta_3} \mathbf{B}_b^T \mathbf{D}^e \mathbf{B}_b d\zeta_2 d\zeta_3 \tag{5}$$

where A is the element area, $\mathbf{D}^e$ and $\mathbf{B}_b$ are the flexural rigidity and strain-displacement matrices of the plate. The integration is calculated using three Gauss points.

The 18 total degrees of freedom (DOFs) of the triangle flat plate/shell element are collected in the nodal displacement vector as

$$\begin{Bmatrix} \mathbf{d}_m \\ \mathbf{d}_b \end{Bmatrix} = \begin{Bmatrix} \{ u_1 \quad v_1 \quad \theta_{z1} \quad u_2 \quad \cdots \quad \theta_{z3} \}^T \\ \{ w_1 \quad \theta_{x1} \quad \theta_{y1} \quad w_2 \quad \cdots \quad \theta_{y3} \}^T \end{Bmatrix} \tag{6}$$

and the stiffness matrix of the flat plate/shell element is

$$[\mathbf{k}]\{\mathbf{d}\} = \begin{bmatrix} [\mathbf{k}_m]_{9\times 9} & \mathbf{0} \\ \mathbf{0} & [\mathbf{k}_b]_{9\times 9} \end{bmatrix} \begin{Bmatrix} \{\mathbf{d}_m\} \\ \{\mathbf{d}_b\} \end{Bmatrix} \tag{7}$$

The geometric stiffness is obtained with an integration using seven Gauss points in the area coordinate system as

$$[\mathbf{k}_\sigma] = \int [\mathbf{G}]^T \begin{bmatrix} \bar{\mathbf{N}} & \mathbf{0} & \mathbf{0} \\ \mathbf{0} & \bar{\mathbf{N}} & \mathbf{0} \\ \mathbf{0} & \mathbf{0} & \bar{\mathbf{N}} \end{bmatrix} [\mathbf{G}] dxdy \tag{8}$$

where $[\bar{\mathbf{N}}]$ is $\begin{bmatrix} N_x & N_{xy} \\ N_{xy} & N_y \end{bmatrix}$ and components of $[\mathbf{G}]$ are derivatives of shape functions with respect to natural coordinates of elements ζ_2 and ζ_3.

2.3.2. Corotational nonlinear analysis

The corotational method [23,25] analyzes elastic deformations of each finite element using the corotational frames by dividing the total element motion into a rigid body motion and an elastic deformation. Fig. 4 shows coordinate systems of a general triangular flat plate/shell element. The initial frame E_0 is defined with a transformation matrix $\mathbf{T}_{E0}$ relating the element coordinate in the undeformed state to the moving body frame that is in turn built in the global frame G. Similarly, the current moving frame E is defined and the corresponding transformation matrix is $\mathbf{T}_E$. The current position $\mathbf{x}^B$ of a node can be obtained from the initial position $\mathbf{X}^B$ in the body frame and a displacement of the node, $\mathbf{u}^B$. Triads S_0 and S are used to describe nodal rotations from the initial configuration to the current one in the body frame. A transformation matrix $\mathbf{T}$ from the nodal triad S_0 to S in the current frame E is given by

$$\mathbf{T} = \mathbf{T}_E^T \mathbf{T}_S \mathbf{T}_{E_0} \tag{9}$$

The transformation matrix $\mathbf{T}_S$ which describes rotations of triad S in the body frame can be updated by assuming $\tilde{\theta}_X$, $\tilde{\theta}_Y$, and $\tilde{\theta}_Z$ are the incremental rotations of triad S in the body frame as [25]

$$(\mathbf{T}_S)_{new} = \tilde{\mathbf{T}} \cdot (\mathbf{T}_S)_{old} \tag{10}$$

where

$$\tilde{\mathbf{T}} = I + \frac{\tilde{\Omega} + 0.5\tilde{\Omega}^2}{1 + 0.25|\omega|^2}, \qquad |\omega| = \sqrt{\tilde{\theta}_X^2 + \tilde{\theta}_Y^2 + \tilde{\theta}_Z^2},$$
$$\tilde{\Omega} = \begin{bmatrix} 0 & -\tilde{\theta}_Z & \tilde{\theta}_Y \\ \tilde{\theta}_Z & 0 & -\tilde{\theta}_X \\ -\tilde{\theta}_Y & \tilde{\theta}_X & 0 \end{bmatrix} \tag{11}$$

The final form of the elastic deformations at the ith node in the current frame E can be expressed as [25]

$$\{\mathbf{d}_i\} = \begin{Bmatrix} \bar{u}_i^{E_1} \\ \bar{u}_i^{E_2} \\ \bar{u}_i^{E_3} \\ \theta_i^{E_1} \\ \theta_i^{E_2} \\ \theta_i^{E_3} \end{Bmatrix}, \quad i = 1, 2, 3 \tag{12}$$

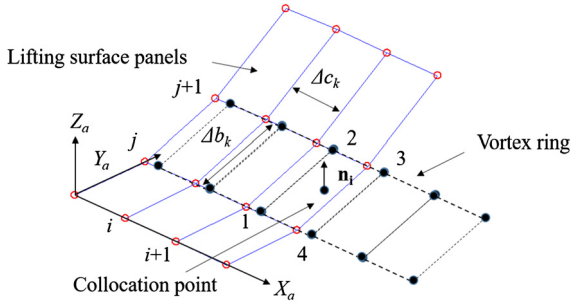

Fig. 5. A vortex ring element on a lifting surface.

where $\bar{u}_i$ and θ_i are the elastic nodal displacements and rotations at the ith node. To eliminate inherent properties of the elastic deformation causing errors in element stiffness calculation, the projection matrix $\mathbf{P}$ [26,27] is applied on nodal deflections $\mathbf{d}$, internal forces $\mathbf{r}$, and element stiffness matrix $\mathbf{k}$:

$$\bar{\mathbf{d}} = \mathbf{P}\mathbf{d}, \quad \bar{\mathbf{r}} = \mathbf{P}^T\mathbf{r}, \quad \bar{\mathbf{k}} = \mathbf{P}^T\mathbf{k}\mathbf{P} \tag{13}$$

Finally, the structural equation to be solved for displacement increments $\Delta\bar{\mathbf{D}}$ is given by

$$[\bar{\mathbf{K}}]\{\Delta\bar{\mathbf{D}}\} = \{\bar{\mathbf{R}}\} \tag{14}$$

where $\bar{\mathbf{K}}$ and $\bar{\mathbf{R}}$ are the assembled current stiffness and load residual. This structural equation can be solved using the Newton-Raphson method.

2.4. Aerodynamic model with unsteady vortex-lattice method

2.4.1. Aerodynamic model with unsteady vortex-lattice method

For the aerodynamic analysis, the unsteady vortex-lattice method (UVLM) [28] is used in the current study. The UVLM assumes the velocity potential and applicable to incompressible flow. In the UVLM, lifting surfaces are modeled as a vortex singularity distribution on the discretized lifting surface panels using bound vortex rings as shown in Fig. 5. Front lines of bound vortex rings for each panel element are located at the quarter-chord position in a panel element, and the collocation points are at the center of the bound vortex rings. Influences of the wake convected from the TE is considered by shed vortex elements. The flow velocity can be solved by using the boundary condition, which is zero normal flow across the wing surface:

$$(\nabla\Phi_B + \nabla\Phi_w + \mathbf{v}) \cdot \mathbf{n} = 0 \tag{15}$$

where $\mathbf{v}$ and $\mathbf{n}$ are the lifting surface velocity and the normal vector to the lifting surface, and Φ_B and Φ_w are the potential of the bound elements and shed wake.

By recalling the Biot-Savart law, the induced flow velocity $\mathbf{w}_{ij}$ on the ith bound vortex influenced by the jth vortex ring is given as

$$\mathbf{w}_{ij} = \bar{\mathbf{w}}_{ij}\Gamma_j \tag{16}$$

where

$$\bar{\mathbf{w}}_{ij} = \sum_{k=1}^{4}\left\{\frac{1}{4\pi}\frac{\mathbf{r}_{mi}\times\mathbf{r}_{ni}}{|\mathbf{r}_{mi}\times\mathbf{r}_{ni}|^2}\mathbf{r}_{0i}\cdot\left(\frac{\mathbf{r}_{mi}}{r_{mi}} - \frac{\mathbf{r}_{ni}}{r_{ni}}\right)\right\}_k \tag{17}$$

where $\mathbf{r}_{mi}$, $\mathbf{r}_{ni}$, and $\mathbf{r}_{0i}$ are position vectors of vortex ring corners on the ith panel as defined in Ref. [28], and $m = 1, 2, 3, 4$ and $n = 2, 3, 4, 1$, which are the vortex ring corner nodes in clockwise order as shown in Fig. 5.

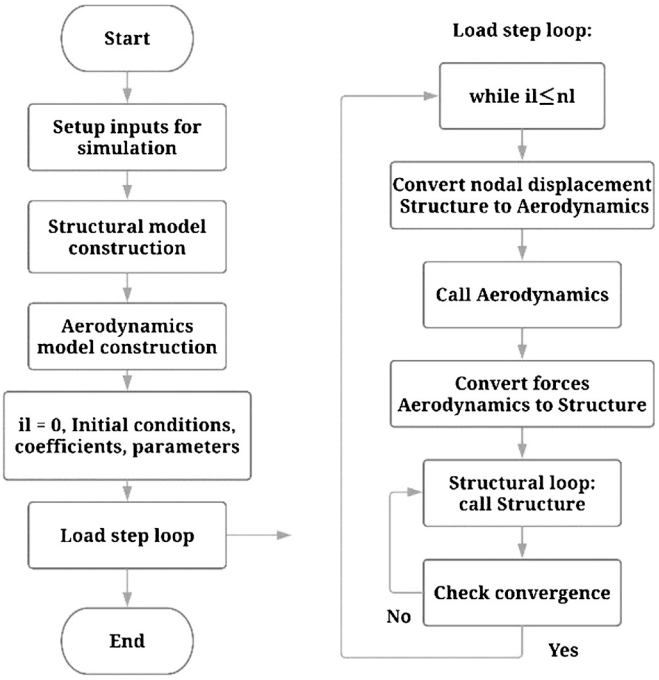

Fig. 6. Procedure of the nonlinear aeroelastic analysis framework.

2.4.2. Aerodynamic loads

The aerodynamic loads can be obtained from the unsteady Bernoulli equation [28]. The pressure difference between upper and lower surfaces Δp_k applied to the kth panel considering both tangential velocities can be given by

$$\Delta p_k = \rho\left\{\left(\mathbf{w}_w(t) + \mathbf{v}(t)\right)_k \cdot \boldsymbol{\tau}_x\frac{\Gamma_{i,j} - \Gamma_{i-1,j}}{\Delta c_k} + \left(\mathbf{w}_w(t) + \mathbf{v}(t)\right)_k \cdot \boldsymbol{\tau}_y\frac{\Gamma_{i,j} - \Gamma_{i,j-1}}{\Delta b_k} + \frac{\partial}{\partial t}\Gamma_k\right\} \tag{18}$$

where ρ is the air density, $\mathbf{w}_w$ is the induced velocity due to the wake which is identical to $\nabla\Phi_w\nabla$, $\boldsymbol{\tau}_x$ and $\boldsymbol{\tau}_y$ are the panel tangential vectors in the X_a and Y_a directions. The Δc_k and Δb_k are the elemental chord and span on the kth panel as shown in Fig. 5. The aerodynamic load on the kth panel is then given by

$$\mathbf{F}_k = -\Delta p_k S_k \mathbf{n}_k \tag{19}$$

where S_k is the panel area.

In addition, a compressibility correction at high subsonic Mach number for UVLM is implemented by following the procedure in Ref. [29] to consider the effect of compressibility.

2.5. Numerical implementation of steady-state solver

In the current nonlinear aeroelastic framework, individual structural and aerodynamic models are explicitly coupled to solve steady-state aeroelastic problems. A flowchart of the aeroelastic simulation is described in Fig. 6.

Two different phases exist in the aeroelastic simulation. The first is a pre- and post-processing block to setup the initial conditions, simulation configuration, and the structural and aerodynamic meshes. Once the initialization is completed, the load step loop starts with the load step counter $il = 0$. The load step loop is divided into two main subroutines: the aerodynamics module to calculate aerodynamic loads based on the UVLM in which a virtual simulation time is set to obtain a converged steady-state value and the structural module to solve the resulting deflection

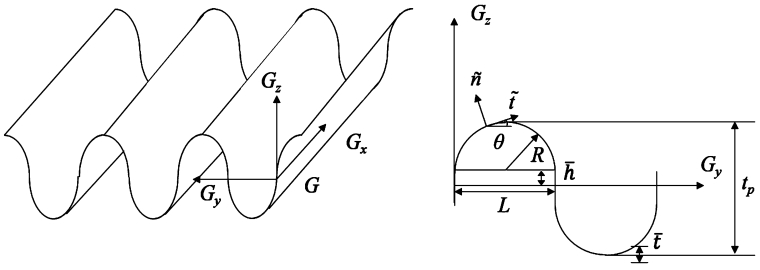

Fig. 7. Definition of the corrugation coordinate systems.

with the corotational approach. Before the aerodynamics module is called, there is the interpolation of structural nodal displacement to the aerodynamic mesh. Also, another interpolation of aerodynamic loads to the structural model is performed ahead of the structural analysis. The geometrically nonlinear structural solver exits when it meets a convergence criterion. Due to the wake shedding method used in the current code, the time step needs to be defined based on the chord length c and the number of chordwise discretization for the lifting panels n_{LSc} as

$$\Delta t = \frac{1}{U_\infty}\left(\frac{c}{n_{LSc}}\right) \tag{20}$$

2.6. Corrugated panel model

The equivalent properties of the periodically corrugated panel in one direction is calculated as a homogeneous orthotropic flat plate by considering the relation between the strain energies and the reaction forces and moments discussed in Ref. [14]. Adaptation of the model to the problem of aeroelastic analysis for a morphing wing with corrugated structure is implemented in this study. Fig. 7 shows a periodic corrugated panel in one direction and the geometry of a round corrugation. Fig. 7 shows two coordinate systems, the global and local frames, which are defined to calculate the corrugated panel properties. With the tangent and normal directions to the laminate, $\tilde{t}$ and $\tilde{n}$, the local coordinate system is defined as shown in Fig. 7. The total thickness of the panel is t_p and the thickness of the composite sheet forming the corrugation is $\bar{t}$.

By neglecting the coupling stiffness matrix **B**, the constitutive relation of the equivalent orthotropic plate is

$$\begin{Bmatrix} \bar{N}_x \\ \bar{N}_y \\ \bar{N}_{xy} \\ \bar{M}_x \\ \bar{M}_y \\ \bar{M}_{xy} \end{Bmatrix} = \begin{bmatrix} \bar{A}_{11} & \bar{A}_{12} & 0 & 0 & 0 & 0 \\ \bar{A}_{12} & \bar{A}_{22} & 0 & 0 & 0 & 0 \\ 0 & 0 & \bar{A}_{66} & 0 & 0 & 0 \\ 0 & 0 & 0 & \bar{D}_{11} & \bar{D}_{12} & 0 \\ 0 & 0 & 0 & \bar{D}_{12} & \bar{D}_{22} & 0 \\ 0 & 0 & 0 & 0 & 0 & \bar{D}_{66} \end{bmatrix} \begin{Bmatrix} \bar{\varepsilon}_x \\ \bar{\varepsilon}_y \\ \bar{\gamma}_{xy} \\ \bar{\kappa}_x \\ \bar{\kappa}_y \\ \bar{\kappa}_{xy} \end{Bmatrix} \tag{21}$$

where $\bar{\varepsilon}_x$, $\bar{\varepsilon}_y$, $\bar{\gamma}_{xy}$, $\bar{\kappa}_x$, $\bar{\kappa}_y$, $\bar{\kappa}_{xy}$ are the strains and curvatures of the orthotropic plate at the mid-plane, and $\bar{N}_x$, $\bar{N}_y$, $\bar{N}_{xy}$, $\bar{M}_x$, $\bar{M}_y$, $\bar{M}_{xy}$ are the forces and moments. The properties $\bar{A}_{ij}$ and $\bar{D}_{ij}$ in Eq. (21) can be expressed as a function of the corrugation geometry. The equivalent stiffness properties of the orthotropic plate can be derived from a periodic Representative Volume Element. In the local coordinate $(\tilde{t}, \tilde{n}, x)$, the constitutive relation of the composite is

$$\begin{Bmatrix} N_t \\ N_x \\ N_{tx} \\ M_t \\ M_x \\ M_{tx} \end{Bmatrix} = \begin{bmatrix} A_{11} & A_{12} & 0 & 0 & 0 & 0 \\ A_{12} & A_{22} & 0 & 0 & 0 & 0 \\ 0 & 0 & A_{66} & 0 & 0 & 0 \\ 0 & 0 & 0 & D_{11} & D_{12} & 0 \\ 0 & 0 & 0 & D_{12} & D_{22} & 0 \\ 0 & 0 & 0 & 0 & 0 & D_{66} \end{bmatrix} \begin{Bmatrix} \varepsilon_t \\ \varepsilon_x \\ \gamma_{tx} \\ \kappa_t \\ \kappa_x \\ \kappa_{tx} \end{Bmatrix} \tag{22}$$

By following the homogenization approach in Ref. [14], equivalent stiffness components can be obtained as

$$\begin{aligned} &\bar{A}_{11} = \frac{\bar{A}_{12}A_{12}}{A_{22}} + \frac{s}{L}\frac{A_{11}A_{22} - A_{12}^2}{A_{22}}, \quad \bar{A}_{12} = \bar{A}_{21} = \frac{A_{12}}{A_{22}}\bar{A}_{22}, \\ &\bar{A}_{22} = \frac{2L}{\frac{I_1}{A_{22}} + \frac{I_2}{D_{22}}}, \quad \bar{A}_{66} = \frac{L}{s}A_{66} \\ &\bar{D}_{11} = \frac{1}{2L}[A_{11}I_2 + D_{11}I_1], \quad \bar{D}_{12} = \bar{D}_{21} = \frac{D_{12}}{D_{22}}\bar{D}_{22}, \\ &\bar{D}_{22} = \frac{L}{s}D_{22}, \quad \bar{D}_{66} = \frac{s}{L}D_{66} \end{aligned} \tag{23}$$

where

$$I_1 = \int_t \left(\frac{dy}{dt}\right)^2 dt, \quad I_2 = \int_t z^2 dt \tag{24}$$

and L and s are the half period and length of a corrugation. Here I_1 and I_2 are functions of the corrugation geometry obtained by Eq. (24). Stiffness components $\bar{A}_{11}$ and $\bar{A}_{22}$ correspond to the extensional stiffness components in the G_x and G_y directions, $\bar{D}_{11}$ and $\bar{D}_{22}$ correspond to the bending stiffness components about the G_y and G_x axes in the global coordinate, and the others follow a similar manner of definition. The equivalent Poisson's ratio is the same as that of the original composite forming the corrugated panel. In case of a round corrugation as shown in Fig. 7, $I_1 = \pi R$, $I_2 = 4\bar{h}^3/3 + 2\pi\bar{h}^2R + 8\bar{h}R^2 + \pi R^3$, $s = \pi R + 2\bar{h}$, and $L = 2R$. Therefore, the properties of corrugated panels can be controlled by the geometric parameters R and $\bar{h}$. On the other hand, if one wants to integrate corrugated structures into wings to achieve the morphing capability, the corrugation geometries have to be constrained by the original wing geometries. In other words, the geometric parameters R and $\bar{h}$ should be determined based on the wing geometries as

$$R = \frac{1}{4}\left(\frac{\Delta c_{cor}}{n_{cor}} - 2\bar{t}\right), \quad \bar{h} = \frac{t_p}{2} - R \tag{25}$$

where Δc_{cor} is the element chord of corrugated panel, n_{cor} is the number of corrugation cycle, and t_p is the thickness between the wing's upper and lower surfaces.

2.7. Spring element

Spring elements are used to provide additional stiffness to the triangular shell elements to analyze performances of highly flexible morphing wings in a fixed morphing shape. The spring element is a simple one-dimensional finite element where its coordinate coincides with the local coordinate of a corresponding triangular element. The spring element can be described with two nodes as shown in Fig. 8. The stiffness of the spring element is given by **k** as [30]

Fig. 8. Simple spring element.

$$\mathbf{k} = \begin{bmatrix} k & -k \\ -k & k \end{bmatrix} \tag{26}$$

where k is the spring constant.

The stiffness components of the spring element are added to the ones of corresponding nodes in a triangular element in which the spring element is integrated.

3. Numerical studies

3.1. Verification of corotational flat plate/shell element

A static analysis is performed to verify the implementation of the flat plate/shell finite element with corotational approach. In the verification case, a cantilever plate made of an isotropic material is loaded at the free edge with an end moment. The flat plate is discretized by 144 triangular flat plate/shell elements and the end moment $M = 56.445$ N m divided into 25 equal steps is applied. The material properties of the plate are Young's modulus $\bar{E} = 196.2$ GPa, shear modulus $\bar{G} = 75.46$ GPa, and Poisson's ratio $\nu = 0.3$. The geometries are thickness $t_p = 0.1$ cm, length $b = 60$ cm, and chord $c = 30$ cm. Analytical solution for the transverse tip deflection can be calculated by

$$w = \frac{\bar{E}I}{M(1-\nu^2)}\left(1 - \cos\frac{Mb(1-\nu^2)}{\bar{E}I}\right) \tag{27}$$

where I is the moment of inertia of the plate.

Fig. 9 shows the vertical tip deflection due to the end moment M. The load history of the plate bending shape is also plotted in Fig. 9. It can be seen that the current model works well.

3.2. Verification of UVLM formulation

For verification purposes of the aerodynamic model, another verification is performed. The simulation result from the current code is compared with a validated result provided in Ref. [28], which is a unsteady response of an impulsively started flat plate at freestream velocity $U_\infty = 50$ m/s with angle of attack α of 5°. Four different rigid flat rectangular wings with chord of 1 m and aspect ratio from 4 to 20 are compared. The rigid wing is discretized by 12 panels along the span and 4 along the chord. The simulations are performed until the lift coefficients converge to the steady-state values. Results show good agreements with the ones given in Ref. [28], as seen in Fig. 10.

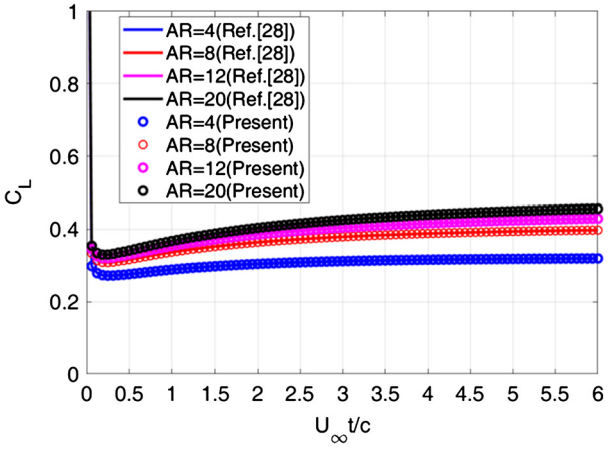

Fig. 10. Lift coefficient of the impulsively started flat rigid wing at $U_\infty = 50$ m/s and $\alpha = 5°$. (For interpretation of the colors in the figure(s), the reader is referred to the web version of this article.)

3.3. Verification of composite and corrugated wing model

A static analysis is then performed to verify the calculation of the composite material properties by comparing with the solution from the commercial FEM software, MSC.Marc. A cantilever composite flat wing made of the orthotropic material, IM7/8552, is loaded at the free edge with a vertical tip load. The composite flat wing has 16-laminated layers. All layers are oriented in 0° along the spanwise direction. The ply thickness is 0.183 mm. The flat plate is discretized by 96 triangular flat plate/shell elements. The end load $F = 10$ N divided into 20 equal steps is applied on each tip node to produce a large deflection. The material properties of IM7/8552 is given in Table 1. The geometries are thickness $t_p = 2.928$ mm, length $b = 2$ m, and width $c = 1$ m. Fig. 11 shows the vertical deflection of the composite flat wing at the elastic axis under the end loads. It shows the good agreement (maximum error at the tip is 3.46%) between the present code and the solution from MSC.Marc.

The implementation of corrugated panel model is also verified by comparing with the values in Ref. [14]. The simulated round-corrugation panel is made of AS4/3501-6 Carbon/Epoxy laminate, whose properties are given in Table 2. The ply angles are [0/90] s. Table 3 shows the values obtained by the current implementation of the corrugated panel model when $R = 3$ mm and $\bar{h} = 3$ mm,

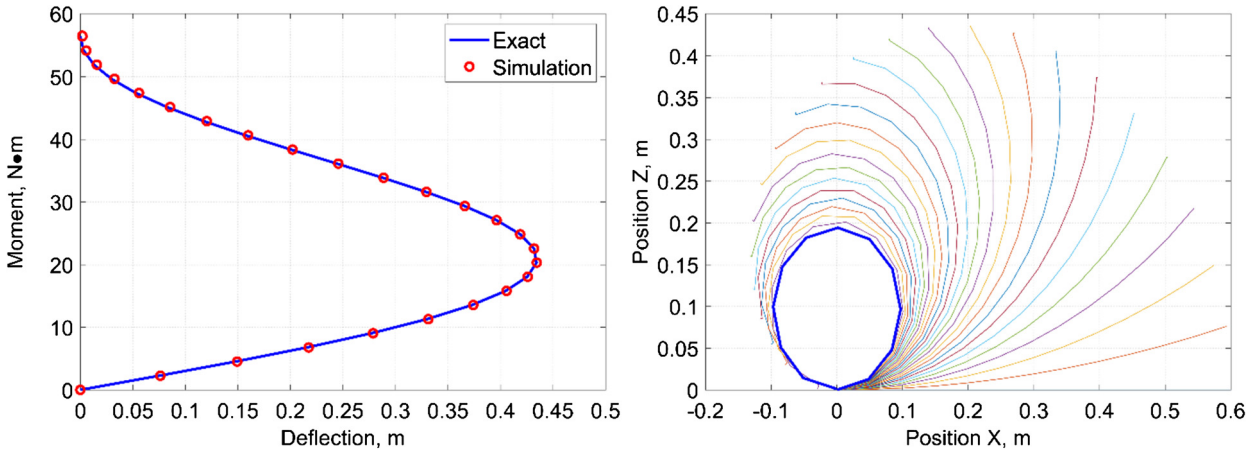

Fig. 9. Vertical tip deflection and applied moment (left) and load history of the bending shape (right).

Table 1
Material properties of IM7/8552.

Property	Value
Axial modulus E_1 (GPa)	171
Transverse modulus E_2 (GPa)	9.10
Poisson's ratio ν_{12}	0.320
Poisson's ratio ν_{23}	0.520
Shear modulus G_{12} (GPa)	5.30
Shear modulus G_{23} (GPa)	3.00

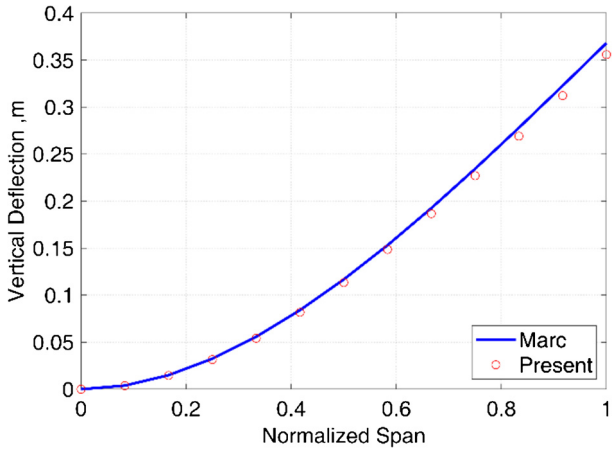

Fig. 11. Vertical deflection of the composite wing with tip loads of 10 N.

Table 2
Material properties of AS4/3501-6.

Property	Value
Axial modulus E_1 (GPa)	148
Transverse modulus E_2 (GPa)	10.5
Poisson's ratio ν_{12}	0.300
Poisson's ratio ν_{23}	0.590
Shear modulus G_{12} (GPa)	5.61
Shear modulus G_{23} (GPa)	3.17

which gives an excellent agreement with the values calculated in Ref. [14].

3.4. Verification of geometrically nonlinear steady-state aeroelastic analysis

A verification of aeroelastic simulation, in which the aerodynamic model is coupled with the structural model, is also performed. Two steady-state aeroelastic simulations are performed with freestream velocities $U_\infty = 5$ and 68.6 m/s, respectively. The altitude is $h = 10{,}000$ m. A flat wing made of steel with chord

Table 3
Stiffness properties for the round corrugation.

Property	Current model	Xia et al. (2012)
$\bar{A}_{11}$ (MN/m)	104.00	104.00
$\bar{A}_{12}$ (kN/m)	1.3536	1.3540
$\bar{A}_{22}$ (kN/m)	34.055	34.055
$\bar{A}_{66}$ (MN/m)	1.1086	1.1090
$\bar{D}_{11}$ (kN m)	1.7103	1.7100
$\bar{D}_{12}$ (N mm)	13.472	13.472
$\bar{D}_{22}$ (N mm)	559.47	559.47
$\bar{D}_{66}$ (N mm)	157.56	157.56

of 1 m, span of 16 m, and thickness of 0.04 m is used, where the wing root angle of attack is $\alpha = 5°$. The material properties of the plate are Young's modulus $\bar{E} = 200$ GPa and Poisson's ratio $\nu = 0.29$. Fig. 12 shows the vertical deflections of the cantilevered wing at the elastic axis (located at the mid-chord) obtained by the current code and steady-state linear solutions. MSC.Nastran SOL144 is used for the linear solutions. The finite element model in the MSC.Nastran consists of 96 triangle elements, which is the same as the current finite element model. At $U_\infty = 5$ m/s with a very small deflection of the wing, there is an excellent agreement between the deflections obtained by the current code and MSC.Nastran. Thus, the current code predicts the small deflection properly. On the other hand, when the wing experiences a large deflection (almost 25% of the wing span) at $U_\infty = 68.6$ m/s, there is a small discrepancy between the vertical deflections in the current nonlinear solution and the linear solution by MSC.Nastran. One contribution of this difference should be the nonlinear stress stiffening. To testify this hypothesis, a simulation result using the geometrically nonlinear structural analysis in the present code with aerodynamic loads calculated by MSC.Nastran, which is the same loads as the "Nastran" case in Fig. 12, is also compared (denoted as "Present Str. + Nastran Aero." in Fig. 12). According to Fig. 12, the stress stiffening due to the large deflection results in the vertical deflection of wing tip 4.23% smaller than the linear solution. In addition, the deformation difference due to the stress stiffening also affects the aerodynamic loads on the wing through different wing twist. For example, the solutions for wing twists on the wing tips are 0.0124 rad in the linear solution and 0.0984 rad in the nonlinear solution. This difference led to the different effective local angle of attack, which also causes different aerodynamic loads as can be seen in Fig. 13. Fig. 13 shows the sectional lifts, drag, and moments on each aerodynamic panel on the leading edge obtained by MSC.Nastran (the doublet-lattice method) and present code (the spanwise node ID is ranging 1 to 12 from the wing root to the tip). The average errors of the sectional lift and moment on the leading edge are 1.94%, respectively. Also, the total error of the lift and moment are 0.87%, respectively. Those differences are attributed to the different effective local angle of

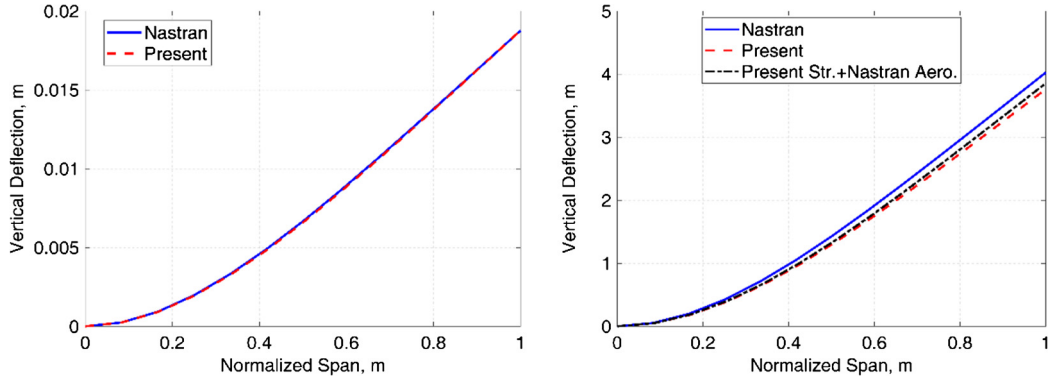

Fig. 12. Vertical deflection of the steel wing at elastic axis at $U_\infty = 5$ (left) and 68.6 (right) m/s and $\alpha = 5°$.

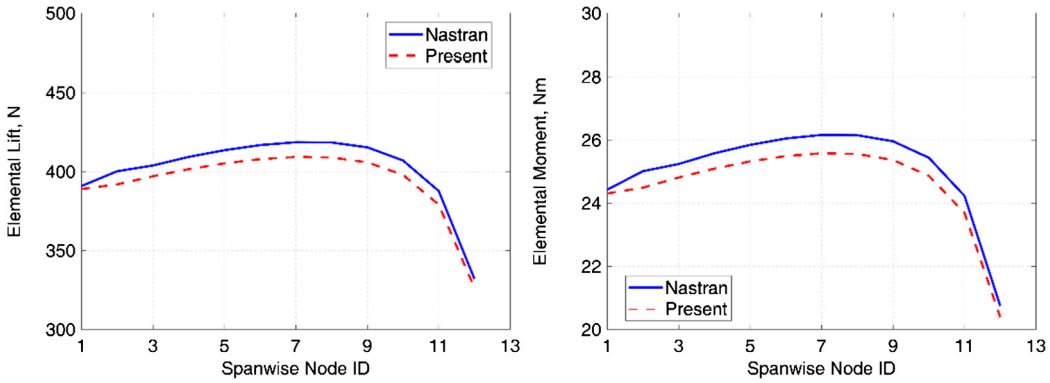

Fig. 13. Lift and drag (left) and moment (right) on aerodynamic panels on leading edge at $U_\infty = 68.6$ m/s and $\alpha = 5°$.

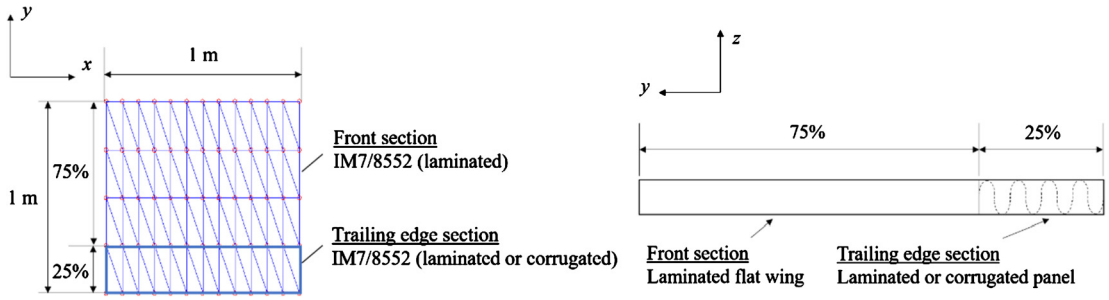

Fig. 14. The planform (left) and cross-section (right) of the flat wing with laminated/corrugated composites.

Table 4
Stiffness properties for the flat plate/shell element with the different round corrugation.

Configuration ID	1	2	3	4	5	6
Number of corrugation cycle	0 (0°)	0 (90°)	50	60	70	100
$\bar{A}_{11}$ (MN/m)	1258.6	66.977	311.91	396.43	497.73	973.40
$\bar{A}_{12}$ (kN/m)	21433	21433	1.2130	0.98963	0.81173	0.44147
$\bar{A}_{22}$ (MN/m)	66.977	1258.6	0.037509	0.030603	0.025102	0.013652
$\bar{A}_{66}$ (MN/m)	38.796	38.796	0.82351	0.64793	0.51607	0.26388
$\bar{D}_{11}$ (N m)	5619.8	299.07	1706.8	2091.2	2548.9	4683.9
$\bar{D}_{12}$ (N mm)	95701	95701	20.314	15.983	12.730	6.5094
$\bar{D}_{22}$ (N m)	299.07	5619.8	0.20466	0.16102	0.12825	0.065580
$\bar{D}_{66}$ (N m)	173.23	173.23	0.81611	1.0373	1.3023	2.5469

attack due to the stress stiffening. The other factor of the discrepancies in the aerodynamic loads is area changes of aerodynamic panels on each iteration during aeroelastic calculations. Since node locations of aerodynamic panels used by the aerodynamic solver in the current analysis framework is updated on every iteration reflecting structural deformations, the aerodynamic panels slightly reduce their size in a situation of these large deflections, while the areas do not change in MSC.Nastran (or can be said that the wing is slightly elongated). Consequently, the present code predicts slightly smaller lifts and moments with large deflections compared MSC.Nastran. Therefore, the current analysis framework seems to capture the steady-state aeroelastic response properly even in the case of large deflection.

3.5. Influence of composite orientation and corrugation parameter onto wings

To demonstrate the capability of the developed nonlinear aeroelastic framework and to have a better understanding of aeroelastic characteristics of corrugated morphing wings, the influence of different composite designs is explored in this section. Fig. 14 shows the flat wing model used in the study. The wing has the chord of 1 m and span of 1 m. The forward area (75% from the LE) is made of IM7/8552 laminate with 40 layers. The ply angles are 0° along the span, the ply thickness is 0.183 mm, and the total thickness of the flat wing t_p is 7.32 mm. Two types of TE design are studied in this paper: laminated and corrugated composites. For the laminated composite cases, the same laminated composite as the forward area is used. The ply angles are 0° or 90° along the span. For the corrugation, a round-corrugation panel made of the same material with 4 layers is used. The ply angles are [0/90]s and the laminate thickness $\bar{t}$ is 0.732 mm for the corrugated panel. The corrugated TE section consists of the corrugated structure to provide the rigidity and flexible upper and lower skins to form the aerodynamics.

First, the equivalent element stiffness properties on the corrugated TE with different numbers of corrugation cycle are calculated as listed in Table 4. The stiffness properties of the laminated composites with the ply angles of 0° and 90° along the span are also shown as zero corrugation (numbers in the parentheses denote the ply angle). In other words, the wing of Configuration ID 1 in Table 4 is a uniform composite wing, whose ply angle is 0° along the span, while the wing of Configuration ID 2 has the ply angle of 90° on the TE section. The cases with 50-, 60-, 70-, and 100-corrugation cycles have the same flat wing thickness t_p as the front section, 7.32 mm. If the laminated composite is directly used as the TE section, the high stiffness properties of the composites in the fiber direction contribute to the corresponding high stiffness

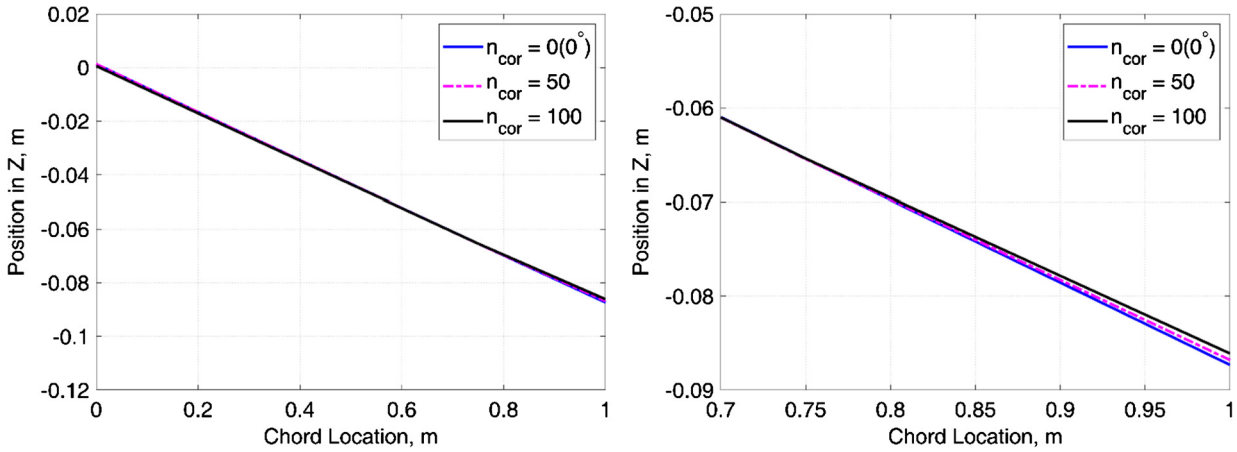

Fig. 15. Shape of the composite wings at wing tip with $U_\infty = 15$ m/s and $\alpha = 5°$.

components in the element. If the laminated composite is used to form the corrugated panel, the extensional stiffness of the panel in the longitudinal direction $\bar{A}_{11}$ increases as the number of corrugation cycle increases. At the same time, the spanwise bending stiffness $\bar{D}_{11}$ also increases with the corrugation cycle increments. On the other hand, the other extensional stiffness properties $\bar{A}_{12}$, $\bar{A}_{22}$, and $\bar{A}_{66}$ decrease with the increase of the corrugation cycle. More importantly, the chordwise bending stiffness $\bar{D}_{22}$ also decreases with the corrugation cycle increments, which contributes to the morphing flexibility of the corrugated panel. Therefore, since the stiffness properties of the wing change corresponding to the change in the number of corrugation cycle, different corrugation numbers can be used to control bending characteristics of wings although a balance between the other stiffness properties should be considered and optimized.

Next, aeroelastic responses of the composite flat wings integrated with the laminated composites or corrugated panels at the TE section (Configuration ID 1, 3, and 6 in Table 4) are investigated to consider an influence of different composite configurations on the wing's aeroelastic responses. The root of the wing is rigidly fixed at the inner three nodes. In other words, the root nodes at the LE and TE are free. The freestream velocity U_∞ is 15 m/s and the altitude h is 10,000 m. The angle of attack is 5°. Fig. 15 shows the shape of the composite wings at the wing tips based on the steady-state aeroelastic simulations. The TE sections of the wings are magnified in the right figure for visibility, showing that the corrugated TEs get larger deflections than the laminate TE does. As can be observed in Fig. 15, the wing of Configuration ID 1 gives the smallest vertical deflection on the TE at the tip among the three cases due to the highest chordwise bending stiffness. The wings with the corrugated TE section of Configuration ID 3 and 6 provide chordwise bending deflection at the TE section on the wing tip due to very low chordwise bending stiffness. The slight nose down deformation can be observed from the wing of Configuration ID 4, which caused by a twist moment created due to the chordwise bending deflection at the TE section of the cantilevered wing.

As can be seen in this study, an aeroelastic response of a composite wing with corrugated structures is influenced by composite and corrugation configurations. Especially with a corrugated TE, the TE may be rolled up during flight due to the low bending stiffness if the corrugation parameter is wrongly set. This may be solved by properly choosing the corrugation parameter and having a balanced chordwise and spanwise bending stiffnesses. Therefore, optimization of corrugation design has to be performed in corrugated structure fabrications and an integrated composite and corrugated wing design. In addition, in an actual wing, a certain mechanism to maintain or control the TE in an optimal angle is required to achieve in-flight wing morphing. For example, a simple wiring system to actuate/control the TE angle presented in Ref. [12, 13] can be implemented. Such a mechanism allows achieving camber morphing with a small number of actuation systems. In the future work, such a control mechanism and wing design to maintain or control the TE angle also need to be studied.

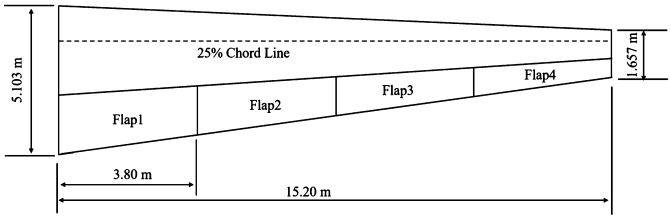

Fig. 16. Wing planform.

3.6. Aeroelastic characteristics of camber morphing wings with corrugated structures

Static aeroelastic characteristics of camber morphing wings with corrugated structures are explored using the present analysis framework. A planform of a tapered wing model used in the study is shown in Fig. 16. A base of the wing model is JAXA Technology Reference Aircraft (TRA) 2012A [31] and the wing is modified for the this study. The chord length of the wing root is 5.103 m, and the chord is linearly narrowed down to 1.657 m at the wing tip without any sweep angle. The semi-span length is 15.2 m, and the aspect ratio is therefore about 9. NACA0012 airfoil is chosen for the following studies. The wing has four trailing edge flaps (the flaps are name as "Flap 1" to "Flap 4" from inner to outer flaps), and the length of each flap is 3.8 m. The wing is cantilevered at the root and divided into 12 elements in the spanwise direction and 10 elements in the chordwise direction, respectively. Performances of two wings with different stiffnesses, rigid and flexible, are studied. The rigid wing is made of aluminum alloy A7075-T6 with Young's modulus $\bar{E} = 71.7$ GPa and Poisson's ratio $\nu = 0.33$. The flexible wing is made of Nylon type 6/6 with Young's modulus $\bar{E} = 28$ GPa and Poisson's ratio $\nu = 0.4$. Also, the performance of corrugated camber morphing flap is compared with a rotational hinged flap as well as without a flap deflection. In this study, Flap 4 with a hinged flap is deflected by 15. A deflection of the corrugated morphing flap is defined so that the vertical deflection of the flap at the trailing edge coincides with the deflection of the hinged flap by following an approach in Ref. [32]. An image of the hinged and corrugated flaps is shown in Fig. 17. The same material as the main section of the wings is used for the hinged flap. The corru-

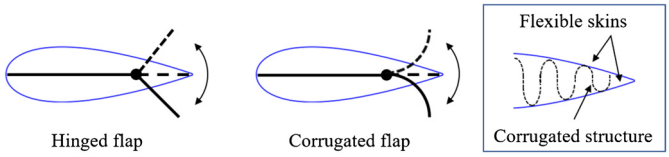

Fig. 17. Hinged and corrugated morphing flaps.

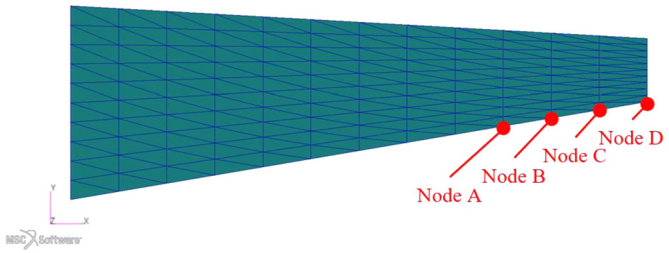

Fig. 18. Node locations of applied moments.

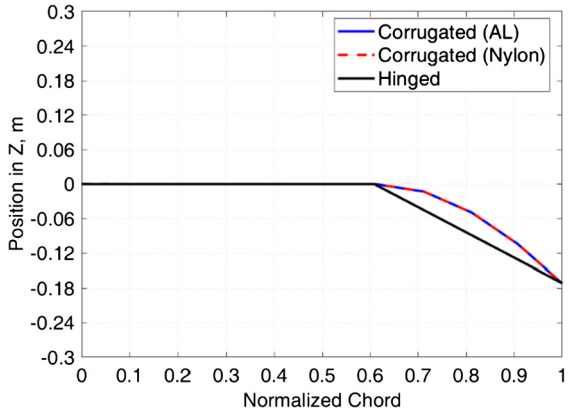

Fig. 19. The outer tip deflection of the hinged and corrugated flaps.

gated morphing flap consists of flexible upper and lower skins and a round-corrugated structure to realize camber morphing. For this study, structural properties of the flexible skins are assumed to be negligible compared with the corrugated structure, and the flexible skins only work to form aerodynamics. The corrugated flap is made of the orthotropic material, IM7/8552. The ply angles of the original laminate constructing the corrugation are [0/90] s, and the laminate thickness is 7.32 mm. The number of corrugation in each shell element of the corrugated flap is 3.

Firstly, a deflection shape of the corrugated flap is obtained by applying moments on the trailing edge of Flap 4 in the current study although a realistic wing morphing will be performed with a certain actuation mechanism, which may not be an edge moment loading. Fig. 18 shows node locations where moments are applied. The applied moments are 37.5 N m on Node A, 77.2 N m on Node B, 118 N m on Node C, and 97 N m on Node D about the x axis. Fig. 19 shows the shapes of wing tip for the hinged and corrugated flaps obtained from a static analysis by the present analysis framework, in which the shapes of the corrugated flap with the rigid and flexible main wing are denoted as “Corrugated (AL) or (Nylon)”, and “Hinged” is the shape of the hinged flap with 15°-deflection.

The current model does not consider a control mechanism for wing morphing of the corrugated trailing edge although corrugated structures, which are highly flexible in the corrugation direction, require a certain mechanism to control/maintain the camber shape under loadings in actual applications. Consequently, rotational spring elements are implemented to maintain the obtained morphing shape on Flap 4. Stiffnesses of 1×10^9 N m/rad about the x axis are used for the spring elements shown in Fig. 20.

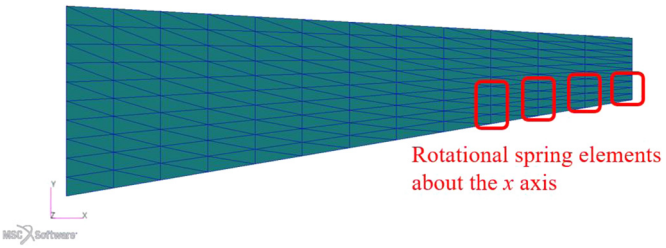

Fig. 20. Locations of additional spring elements.

In the following simulations, the free stream velocity U_∞ is 180 m/s, the altitude h is 500 m, and the wing root angle of attack α is 5°. Rigid wings made of the aluminum alloy with three flap configurations are firstly studied. The wing tip vertical deflections on the mid-chord line with the three configurations and the lift distributions on the trailing edge of Flap 4 with hinged and corrugated flaps are shown in Fig. 21. Both hinged and corrugated flap deflections gave increased lift in the region of the flaps leading the larger vertical deflections compared to the wing without any flap deflection. Moreover, the highest lift of the rigid wing with the corrugated flap at normalized span of 0.9 was increased by 118% compared to the lift at the same location of the rigid wing with the hinged flap. The larger lift in the region of the corrugated flap led to a slightly larger vertical deflection compared to the rigid wing with the hinged flap by 5.13% at the wing tip.

Flexible wings made of the nylon with three flap configurations are then analyzed. Fig. 22 shows the wing vertical deflection and the lift distribution. The corrugated flap with the flexible wing also produced larger lift than the hinged flap by 115% at the normalized span of 0.9. However, the vertical deflections on the flexible wings with the hinged and corrugated flap deflections are very close. This is mainly because the major portions of the wing are highly flexible. The camber lines at the tips of wings with aluminum and nylon are shown in Fig. 23. The major portion of the flexible wing with the corrugated flap was twisted due to the large lift generated in the region of the flap causing a reduction of effective local angle of attack. Consequently, the total lift on the flexible wing with the corrugated flap was not increased as can be seen in Fig. 24 although the flexible wing with the corrugated flap can produced larger lift around the flap. Fig. 24 shows the distributions of chordwise total lift along the span for rigid and flexible wings. The total lift of the rigid wing with the corrugated flap was increased by 1.71% compared with the wing having the hinged flap, while the total lift of the flexible wing with the corrugated flap was actually 0.52% lower than the total lift of the wing with the hinged flap. Hence, wing designs with corrugated morphing flaps need to be optimized with respect to an overall balance of aeroelastic characteristics, especially for flexible wings although a camber morphing wing with corrugated structures can provide larger local lift.

4. Conclusions

In this paper, an integrated geometrically nonlinear aeroelastic framework to analyze the steady-state nonlinear aeroelastic response of morphing composite wing with orthotropic materials has been developed. The objectives of this paper were 1) to develop an integrated geometrically nonlinear aeroelastic framework, which allows studying corrugated morphing wings, 2) to verify the developed analysis framework, and 3) to demonstrate the capability of the framework and explore the influence of different corrugated morphing wing designs on aeroelastic responses as well as the aeroelastic characteristics of the corrugated camber morphing wing. For the structural model, a corotational approach with a flat plate/shell finite element was used to take into account the geometrical nonlinearity due to the large deformation of

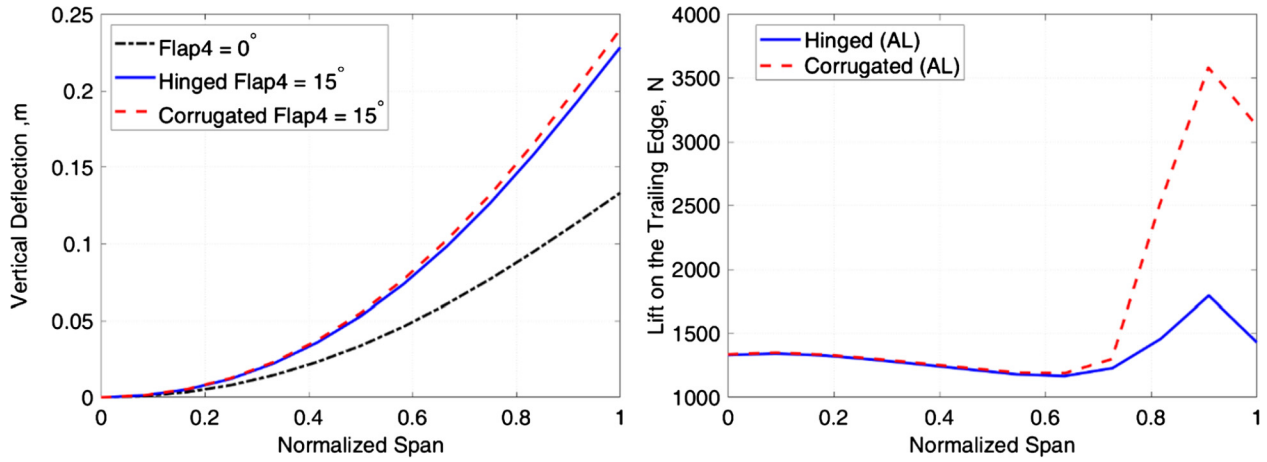

Fig. 21. Wing tip vertical deflections on the mid-chord (left) and lift distributions on the trailing edge of Flap 4 with hinged and corrugated flaps for the rigid wings.

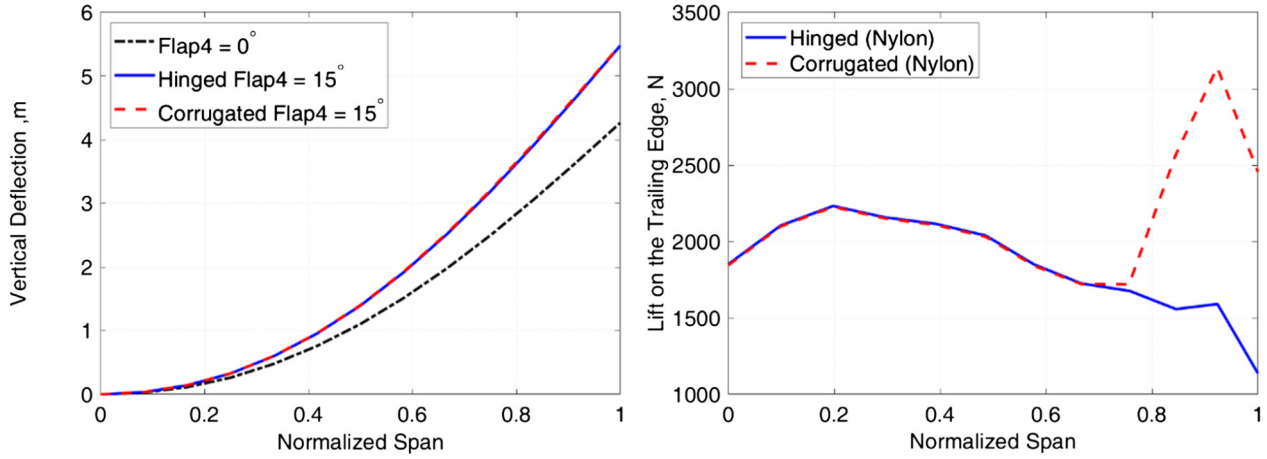

Fig. 22. Wing tip vertical deflections on the mid-chord (left) and lift distributions on the trailing edge of Flap 4 with hinged and corrugated flaps for the flexible wings.

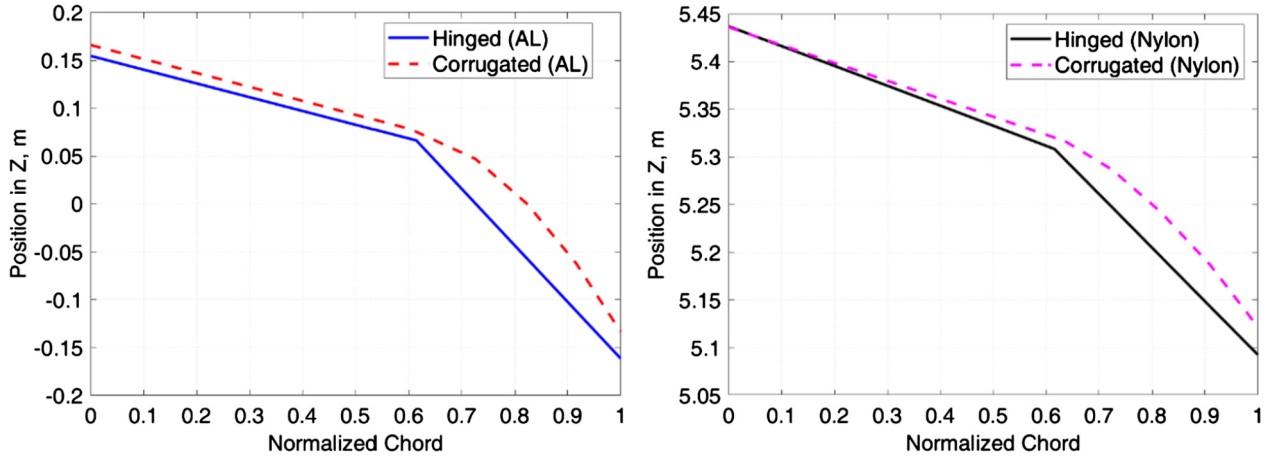

Fig. 23. The cross-sections of the wing tips with aluminum alloy (left) and nylon (right).

morphing wing. A UVLM formulation has also been implemented and coupled with the structural part. The integrated geometrically nonlinear aeroelastic framework also provided the capability to investigate the influence of different materials and structures. The present code allows studying the aeroelastic response of both isotropic and orthotropic materials. The response of a corrugated structure, which is compatible with a camber morphing wing, can also be analyzed by approximating the structure as an equivalent orthotropic panel with a homogenization method. In addition, the spring element is implemented in the structural solver for additional modeling capability.

The developed analysis modules including the corotational structural model, aerodynamics model with UVLM, and equivalent corrugated panel model were verified by comparing with analytical solutions or other experimentally validated models. The nonlinear aeroelastic analysis also provided reasonable accuracy.

Numerical studies in this paper explored influences of composite and corrugated structures on the static aeroelastic behaviors of

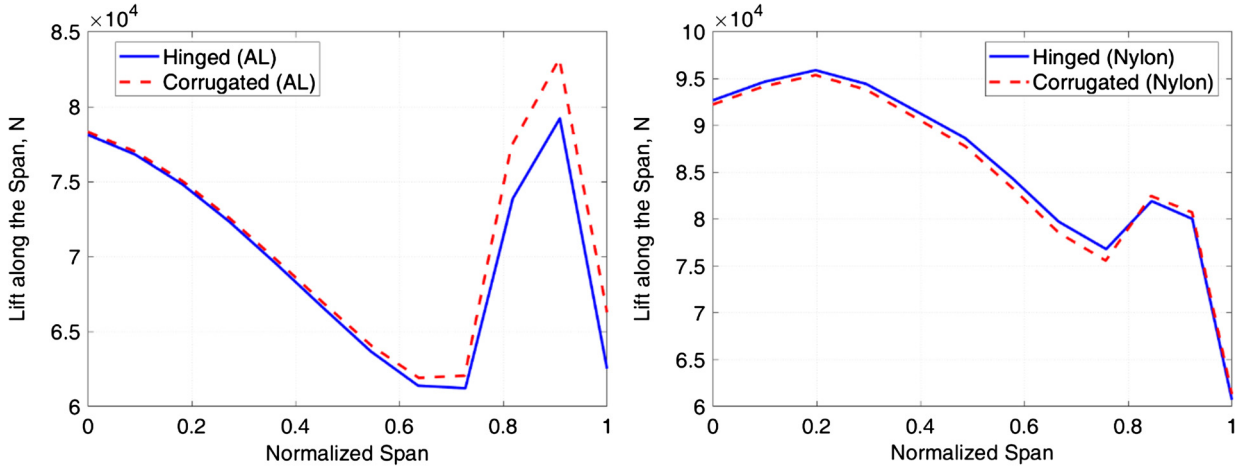

Fig. 24. Distributions of chordwise summations of the elemental lift along the span for rigid (left) and flexible (right) wings.

a composite flat wing with a corrugated structure by using the developed aeroelastic analysis framework. Since the aeroelastic characteristics of composite and corrugated wings are highly impacted by composite and corrugation parameters, optimization of design parameters of composites and corrugations should be performed. The aeroelastic characteristics of camber morphing wings with corrugated structures were also explored with the aeroelastic framework. Tapered rigid and flexible wings with three different flap configurations, which were not deflected, hinged, and corrugated morphing flaps, were studied. The corrugated flap could provide a performance as a high-lift device. However, such local high-lift might create a different aeroelastic response to a wing and not always achieve the increase of total lift on a wing, especially in case of a flexible wing. Therefore, when a conventional hinged flap is replaced by a corrugated morphing flap, wing designs have to be optimized with respect to overall aeroelastic performance.

In future works, although the verification of the current nonlinear aeroelastic framework is performed by comparing with linear solutions with flat plates/shells elements in this paper, a direct comparison with other nonlinear solutions with flat plates/shells elements or experimental results should be performed. Also, a detailed study of flexible skins such as effects of additional stiffness and vibrations of thin skins for the corrugated morphing wing will be performed for accurate investigations of morphing wing designs. In addition, a certain actuation mechanism to maintain the TE angle of corrugated wings, such as wire and actuator system, needs to be considered. With the actuator system implemented, aerodynamic and aeroelastic characteristics of corrugated wings will be investigated. An optimal design of the integrated morphing wing with corrugated structures will also be studied. Finally, the analysis will also be extended for a time-domain analysis to fully utilize the unsteady aerodynamics model and complete the nonlinear and unsteady aeroelastic framework.

Conflict of interest statement

There is no conflict of interest.

Acknowledgements

This work was conducted under the financial support of Grant-in-Aid for Scientific Research (No. 15K06598) by Japan Society for the Promotion of Science.

References

[1] E. Pendleton, P. Flick, D. Paul, D.F. Voracek, E. Reichenbach, K. Griffin, The X-53 a summary of the active aeroelastic wing flight research program, in: 48th AIAA/ASME/ASCE/AHS/ASC Structures, Structural Dynamics and Materials Conference and Exhibit, Honolulu, HI, Apr. 23–26, 2007, AIAA Paper 2007-1855.

[2] S.B. Cumming, M.S. Smith, A. Ali, T.T. Bui, J. Ellsworth, C.A. Garcia, Aerodynamic flight test results for the adaptive compliant trailing edge, in: AIAA Atmospheric Flight Mechanics Conference, Washington, DC, Jun. 13-17, 2016, AIAA Paper 2016-3855.

[3] M.S. Smith, T.T. Bui, C.A. Garcia, S.B. Cumming, Longitudinal aerodynamic modeling of the adaptive compliant trailing edge flaps on a GIII aircraft and comparisons to flight data, in: AIAA Atmospheric Flight Mechanics Conference, Washington, DC, June 13-17, 2016.

[4] N. Nguyen, S. Lebofsky, E. Ting, U. Kaul, D. Chaparro, J. Urnes, Development of variable camber continuous trailing edge flap for performance adaptive aeroelastic wing, in: SAE 2015 AeroTech Congress and Exhibition, SAE International, Seattle, WA, Sep. 22–24, 2015.

[5] F. Afonso, J. Vale, F. Lau, A. Suleman, Performance based multidisciplinary design optimization of morphing aircraft, Aerosp. Sci. Technol. 67 (2017) 1–12.

[6] U.K. Kaul, N.T. Nguyen, Drag optimization study of variable camber continuous trailing edge flap (VCCTEF) using OVERFLOW, in: 32nd AIAA Applied Aerodynamics Conference, Atlanta, GA, June 16-24, 2014, AIAA Paper 2014-2444.

[7] N. Tsushima, W. Su, Concurrent active piezoelectric control and energy harvesting of highly flexible multifunctional wings, J. Aircr. 54 (2016) 724–736.

[8] N. Tsushima, W. Su, Flutter suppression for highly flexible wings using passive and active piezoelectric effects, Aerosp. Sci. Technol. 65 (2017) 78–89.

[9] N. Tsushima, W. Su, Modeling of highly flexible multifunctional wings for energy harvesting, J. Aircr. 53 (2016) 1033–1044.

[10] N. Tsushima, W. Su, A study on adaptive vibration control and energy conversion of highly flexible multifunctional wings, Aerosp. Sci. Technol. 79 (2018) 297–309.

[11] T. Yokozeki, S. Takeda, T. Ogasawara, T. Ishikawa, Mechanical properties of corrugated composites for candidate materials of flexible wing structures, Composites, Part A, Appl. Sci. Manuf. 37 (2006) 1578–1586.

[12] H. Takahashi, T. Yokozeki, Y. Hirano, Development of variable camber wing with morphing leading and trailing sections using corrugated structures, J. Intell. Mater. Syst. Struct. 27 (2016) 2827–2836.

[13] T. Yokozeki, A. Sugiura, Y. Hirano, Development of variable camber morphing airfoil using corrugated structure, J. Aircr. 51 (2014) 1023–1029.

[14] Y. Xia, M.I. Friswell, E.I.S. Flores, Equivalent models of corrugated panels, Int. J. Solids Struct. 49 (2012) 1453–1462.

[15] Y.S. Jung, D.O. Yu, O.J. Kwon, Aeroelastic analysis of high-aspect-ratio wings using a coupled CFD-CSD method, Trans. Jpn. Soc. Aeronaut. Space Sci. 59 (2016) 123–133.

[16] S.K. Chimakurthi, B.K. Stanford, C.E. Cesnik, W. Shyy, Flapping wing CFD/CSD aeroelastic formulation based on a corotational shell finite element, in: 50th AIAA/ASME/ASCE/AHS/ASC Structures, Structural Dynamics, and Materials Conference, Palm Springs, CA, May 4–7, 2009.

[17] H. Arizono, C.E. Cesnik, Computational static aeroelasticity using nonlinear structures and aerodynamics models, in: 54th AIAA/ASME/ASCE/AHS/ASC Structures, Structural Dynamics, and Materials Conference, Boston, MA, Apr. 8–11, 2013, AIAA Paper 2013-1862.

[18] M. Winter, F.M. Heckmeier, C. Breitsamter, CFD-based aeroelastic reduced-order modeling robust to structural parameter variations, Aerosp. Sci. Technol. 67 (2017) 13–30.

[19] C. de Souza, R.G. da Silva, C. Cesnik, Nonlinear aeroelastic framework based on vortex-lattice method and corotational shell finite element, in: 53rd AIAA/ASME/ASCE/AHS/ASC Structures, Structural Dynamics and Materials Conference, Honolulu, HI, Apr. 23–26, 2012.

[20] W. Su, Y. Huang, J.R. Hammerton, Nonlinear aeroelasticity of highly flexible joined-wing aircraft using unsteady vortex-lattice method, in: 58th AIAA/ASCE/AHS/ASC Structures, Structural Dynamics, and Materials Conference, Grapevine, TX, Jan. 9–13, 2017.
[21] M.J. Smith, D.H. Hodges, C.E.S. Cesnik, Evaluation of computational algorithms suitable for fluid-structure interactions, J. Aircr. 37 (2000) 282–294.
[22] C.A. Felippa, A study of optimal membrane triangles with drilling freedoms, Comput. Methods Appl. Math. 192 (2003) 2125–2168.
[23] P. Khosravi, R. Ganesan, R. Sedaghati, Corotational non-linear analysis of thin plates and shells using a new shell element, Int. J. Numer. Methods Eng. 69 (2007) 859–885.
[24] J.L. Batoz, K.J. Bathe, L.W. Ho, A study of three-node triangular plate bending elements, Int. J. Numer. Methods Eng. 15 (1980) 1771–1812.
[25] C. Rankin, F. Brogan, An element independent corotational procedure for the treatment of large rotations, J. Press. Vessel Technol. 108 (1986) 165–174.
[26] B. Nouromid, C.C. Rankin, Finite rotation analysis and consistent linearization using projectors, Comput. Methods Appl. Math. 93 (1991) 353–384.
[27] C.C. Rankin, B. Nouromid, The use of projectors to improve finite-element performance, Comput. Struct. 30 (1988) 257–267.
[28] J. Katz, A. Plotkin, Low-Speed Aerodynamics, Cambridge University Press, Cambridge, UK, 2001, pp. 230–447.
[29] T. Melin, A.T. Isikveren, M.I. Friswell, Induced-drag compressibility correction for three-dimensional vortex-lattice methods, J. Aircr. 47 (2010) 1458–1460.
[30] P.I. Kattan, The Spring Element, MATLAB Guide to Finite Elements: An Interactive Approach, Springer, Berlin, Heidelberg, 2008, pp. 11–26.
[31] D. Kwak, M. Tamayama, T. Nomura, H. Arizono, Preliminary studies on the lift distribution and aspect ratio of subsonic aircraft wing for fuel consumption reduction, in: 53rd JSASS Aircraft Symposium, JSASS, Toyama, Japan, 2015.
[32] B. Sanders, F.E. Eastep, E. Forster, Aerodynamic and aeroelastic characteristics of wings with conformal control surfaces for morphing aircraft, J. Aircr. 40 (2003) 94–99.